RESEARCH

Characterization of a scintillating lithium glass ultra-cold neutron detector

Blair Jamieson[1][*], Lori A Rebenitsch[1], Sean Hansen-Romu[1], Bernhard Lauss[2], Thomas Lindner[3,1], Russ Mammei[1], Jeff W Martin[1] and Edgard Pierre[4,3]

Abstract

A new ^{6}Li glass based scintillation detector developed for the TRIUMF neutron electric dipole moment experiment was characterized using the ultra-cold neutron source at the Paul Scherrer Institute (PSI). The data acquisition system for this new detector was demonstrated to perform well at rejecting backgrounds. An estimate of the absolute efficiency of background rejection is made as a function of rate. For the variable ultra-cold neutron rate (varying from < 1 kHz to approx. 100 kHz per channel) and background rate seen at the Paul Scherrer Institut, we estimate that the absolute detector efficiency is $89.7^{+1.3}_{-1.9}\%$ and the background contamination is $0.3 \pm 0.1\%$. Finally a comparison with a commercial Cascade detector was performed for a specific setup at the West-2 beamline of the ultra-cold neutron source at PSI.

Keywords: ^{6}Li; UCN detector; Ultra-cold neutrons

1 Introduction

Determining the neutron Electric Dipole Moment (nEDM) limits theories beyond the Standard Model [1]. Ultra-Cold Neutrons (UCN) provide a good means to search for a nEDM. As a result, there are various nEDM experiments around the world utilizing UCN that are either running or being planned [2–11]. Measurements are limited mainly by UCN statistics. Increasing the efficiency of the detection system is therefore important.

The UCN source at the Research Centre for Nuclear Physics (RCNP) in Osaka successfully demonstrated UCN production in super-fluid helium and extraction through cold windows in 2013 [12]. This source is in the process of being moved from RCNP to TRIUMF, in Vancouver, over the coming year where a new UCN facility is being prepared. A neutron Electric Dipole Moment (nEDM) experiment is planned as the first experiment after the source will be installed at TRIUMF [13].
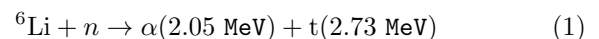
A UCN detector using ^{6}Li glass has been designed and built for the nEDM experiment. This detector must fulfill several performance requirements, including the ability to dependably count UCN at high rates (> 1 MHz). In order to determine the detector's performance, the detector has been bench-marked against a Cascade UCN detector[1] using the UCN source at the Paul Scherrer Institute (PSI) in Switzerland [14–16].

This paper will describe the ^{6}Li based scintillation detector in Section 2. One goal of the tests is to estimate the overall detection efficiency and background rejection capabilities of the ^{6}Li detector. In order to understand the efficiency and background rejection due to Pulse Shape Discrimination (PSD) used to reject backgrounds for the ^{6}Li detector, a simulation of the UCN detection and background detection was prepared, as described in Section 3. To get an estimate of the absolute detector efficiency, described in Section 4, we have taken account of the PSD cut efficiency, along with estimates of the geometrical acceptance, and neutrons lost to the lithium depleted layer of glass on top of the detector. A comparison of the detector measurement to a Cascade UCN detector is described in Section 5. As the detectors reach higher detection rates, the effects of pile-up and electronics dead-time need to be estimated, as detailed in Appendix A.

2 Overview of Detector Technology

2.1 ^{6}Li Scintillating Glass Detector

The scintillating glass is doped with ^{6}Li, which has a high neutron capture cross-section of order 10^5 b. The charged particles in the reaction:

$$^6\text{Li} + n \rightarrow \alpha(2.05 \text{ MeV}) + \text{t}(2.73 \text{ MeV}) \tag{1}$$

[*]Correspondence: bl.jamieson@uwinnipeg.ca
[1] Department of Physics, University of Winnipeg, 515 Portage Avenue, Winnipeg, Canada
Full list of author information is available at the end of the article

[1]CD-T Technology, Hans-Bunte Strasse 8-10, 69123 Heidelberg, Germany

are detected.

In order to reduce the effect of an α or triton escaping the glass, two optically-bonded pieces of scintillating glass are used. This type of scintillating stack detector was pioneered by the group at LPC Caen [17–20]. The upper layer is depleted of ^{6}Li (GS30) and the lower layer is doped with ^{6}Li (GS20) to allow the resultant particles to deposit their full energy within the scintillating glass[2]. Optical contacting of the two layers was performed by Thales-Seso in France, and a method of checking the doped side of the glass was developed at the University of Winnipeg [21]. The scintillation light is then guided via ultra-violet transmitting acrylic light-guide to its corresponding photomultiplier tube outside the detector vacuum region. The scintillation following neutron capture gives a fast event signal with rise time of 6 ns and a fall time of about 40 ns. There is also a slower decaying light component up to 2 μs.
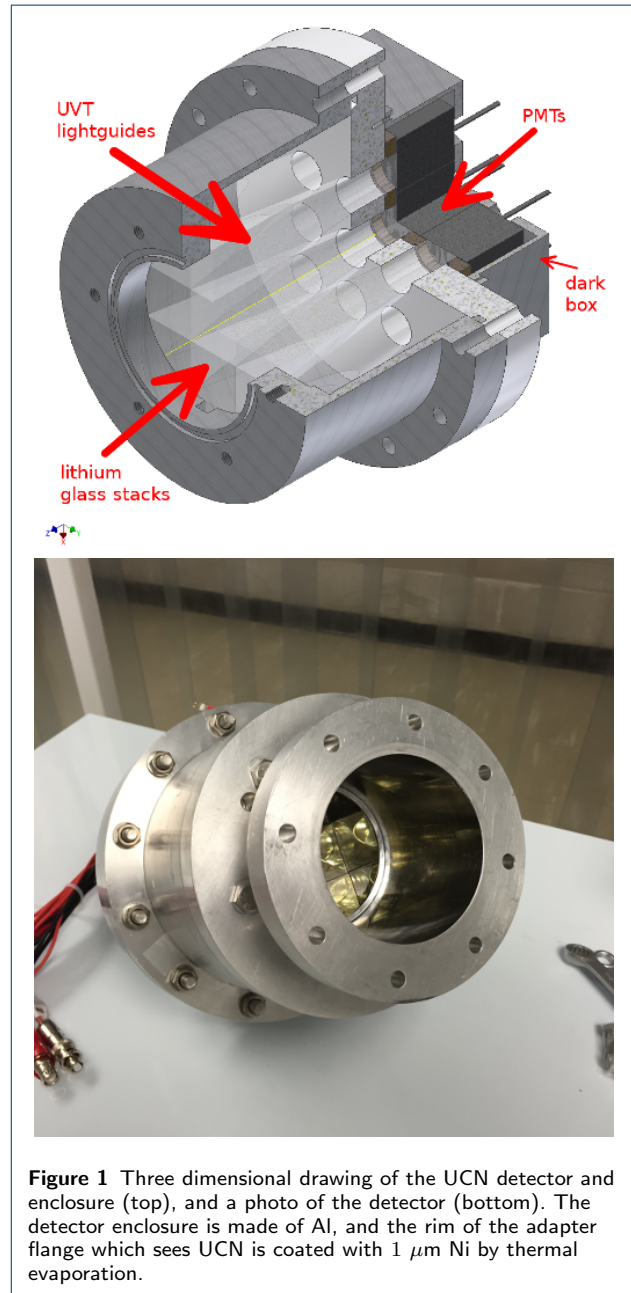
The detector design is similar to the detector developed for the nEDM experiment at PSI, and also employed at PSI for UCN monitoring [22]. These detectors have some sensitivity to gamma-ray and thermal neutron backgrounds. Background contamination will be discussed further in the paper in Sections 3.1 and 4.3. Making the scintillating Li glass as thin as possible reduces this sensitivity to both thermal neutron captures and to γ-ray backgrounds. Thinner than about 50 μm would also result in an efficiency loss as the charged particles produced in the neutron capture could begin to escape the glass before stopping. In addition, the gamma rays producing scintillation light or via Cerenkov effect in the light-guides can be rejected by Pulse-Shape Discrimination (PSD) since these signals do not have a slow decaying component and are therefore shorter (FWHM approx. 20 ns) than the scintillation signal from the lithium glass.

In order to handle the expected high UCN rates, the ^{6}Li detector face is segmented into 9 channels. This reduces pile-up. A photograph and a drawing of the detector are show in Figure 1. The entire enclosure was machined from Al, and an adapter flange which has a rim which see UCN was coated with natural abundance Ni. The ^{6}Li glass tile side lengths of 29 mm, and opening on the adapter flange of 81 mm on the front face of the photograph can be used as a reference scale for the detector size.

2.2 ^{6}Li Detector Signal Treatment

Each of the nine tiles of scintillating glass's light is detected by a Hamamatsu R7600U Photomultiplier Tube

Figure 1 Three dimensional drawing of the UCN detector and enclosure (top), and a photo of the detector (bottom). The detector enclosure is made of Al, and the rim of the adapter flange which sees UCN is coated with 1 μm Ni by thermal evaporation.

[2]GS20 and GS30 were purchased from Applied Scintillation Technologies, now Scintacor, 8 Roydonbury Industrial Estate, Horsecroft Road, Harlow, CM19 5BZ, United Kingdom

(PMT). The signals from the PMTs are amplified by a Phillips 775 Octal $10\times$ Preamplifier and read out by an 8-channel CAEN V1720 digitizer.

The CAEN V1720 has a PSD firmware that will online, find pulses above a certain threshold and calculate background rejection quantities. The firmware stores only the minimal necessary information about every found pulse, thereby permitting the V1720 to handle data rates above MHz without saturating the data path. The first seven tiles of the detector are read out on one digitizer, and the last two tiles are read out on a second digitizer. Each of the digitizers was connected by an independent optical fibre to a CAEN A3818 PCI card on the Data Acquisition (DAQ) computer for readout, allowing data rates up to 85 MB/s.

The time-stamp provided by the digitizer is a clock cycle count in 4 ns ticks up to 17 seconds. To help keep track of the time-stamp wrap-around, and check the digitizer synchronization, a 1 Hz pulser was fed into the last channel of each of the two digitizers. In addition a signal from the PSI proton beam timing was sent into one of the channels of the detector to be used to determine the times when the proton beam arrived.

The DAQ software used the MIDAS system that is commonly used at PSI and TRIUMF. A MIDAS frontend for the CAEN V1720 was written to collect the PSD data from the digitizers and save it into MIDAS banks.

Further details on the digitizer PSD settings can be found in Section 3.1.

3 Scintillation and light-guide background simulation

In order to build probability distribution functions for late light events, multiple signal events, and combinations of signal and background events, a detailed simulation of the voltage pulses from the lithium glass and of the digitizer PSD was developed. A single photoelectron (p.e.) was assumed to produce a Gaussian pulse with an amplitude drawn from a Gaussian with mean and width, $A = 20$ mV, with a minimum amplitude for a single p.e. as 4 mV.

A single scintillation signal event's pulse was then built assuming that the arrival times of each photoelectron from the scintillation signal followed a rise time, $\tau_R = 6.4$ ns, a fast scintillation fall time, $\tau_F = 41.7$ ns, and a slow scintillation fall time, $\tau_S = 2000$ ns. The probability, $P(t)$, of having a photo-electron at a given time, t, when the scintillation light starts arriving at time, T, was drawn from the distribution:

$$P(t) = \begin{cases} A(1 - e^{-(t-T)/\tau_R}), & T < t < T + 5\tau_R \\ A((1 - f_L)e^{-(t-T-5\tau_R)/\tau_F} + \\ f_L e^{-(t-T-5\tau_R)/\tau_L}), & t >= T + 5\tau_R. \end{cases} \quad (2)$$

The fraction of the scintillation light in the late light was $f_L = 1\%$. All of the values used in the simulation, as described above, were chosen to best match the data. The number of photo-electrons for a single neutron event was drawn from a Poisson distribution with a mean number of photo-electrons of 83 to match the mean over sigma of the total charge, Q_L, distribution from data. The distribution of scintillation photo-electron arrival times along with a sample pulse is shown in the left panel of Fig. 2.
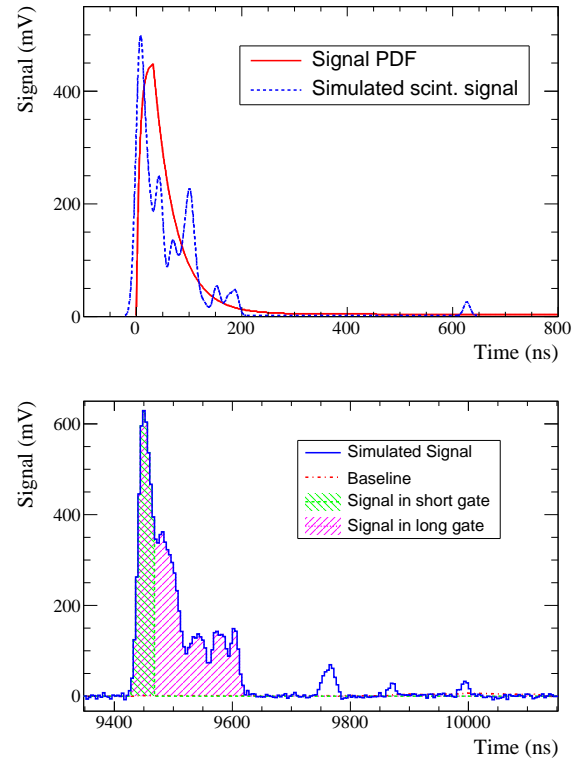
Figure 2 Simulated scintillation signal (blue dashed) and distribution function used to generate it (red solid) is shown in the top panel. The bottom panel shows the digitizer treatment of another simulated signal (solid line), where the baseline calculation (red dot-dashed line), signal within the short gate (green right-diagonal fill) and signal within the long gate (magenta left-diagonal fill) are shown.

A single background event was modelled as having a Gaussian pulse with $\sigma = 6.4$ ns for the times of each photo-electron. Again, each photo-electron was treated as a Gaussian with a random amplitude drawn from a Gaussian with mean and width of $A = 20$ mV, and accepting only amplitudes above 4 mV. The number of photo-electrons for the background signal was drawn from an exponential distribution with an average of 7.5 photo-electrons. This distribution was chosen to match the dominant component of the background observed in data.

The simulation of the pulses was used to generate 0.1 second long sets of data where the signal and background pulses were generated at a specified random rate. These simulated data were then sent to a digitizer simulation, described in the following section.

3.1 Digitizer simulation

The CAEN V1720 digitizer with the PSD firmware samples the waveforms every 4 ns, and for each sample digitizes the voltage on a 2 V scale into an ADC value between 0 and 4096. Each channel of the digitizer can trigger on its signal based on going some number of ADC counts below a pedestal value. In the simulation the threshold was set at 250 ADC ($\sim$ 125 mV). The digitizer can be run with a fixed pedestal, or a pedestal taken from an average over the last 32 samples which is simpler to set up. This self calculated pedestal is called a baseline in the digitizer documentation, and once a trigger happens, the baseline is held constant until the end of a specified gate time.

The PSD firmware calculates the sum of the signal below the threshold for a short gate width, $t_s = 40$ ns, and for a long gate width, $t_L = 200$ ns, after the trigger. The ADC sum below threshold within the short gate is called, Q_S, and the sum within the long gate is called, Q_L. The PSD value is also calculated, and defined as:

$$\mathrm{PSD} = \frac{(Q_L - Q_S)}{Q_L}. \tag{3}$$

After each trigger, the digitizer channel is busy for a 150 ns dead-time. An example of the signal within each of the gates is depicted in the right panel of Fig. 2. A cut on the values of the charges Q_L and PSD provides a rejection of gamma interactions with the light-guides.

Seven categories of events are considered: single neutrons (1n), and single backgrounds (1γ), pile-up of multiple signal neutrons (Nn), pile-up of multiple backgrounds (Nγ), pile-up of a single neutron with a background (1n1γ), signal neutrons which happen during the digitizer dead-time (1n deadtime), and re-triggers on late light from the scintillator (0n0γ). Simulated electronic pulses for each of these possible combinations are shown in Fig. 3 and Fig. 4.

3.2 Probability distribution functions from the simulations

The combination of the signal and background pulse simulations with the digitizer simulation is used to generate Probability Distribution Functions (PDFs) in the PSD versus Q_L space for each of the different possible combinations of events.

To limit the number of possible PDFs, an approximation of the higher event multiplicities within a single
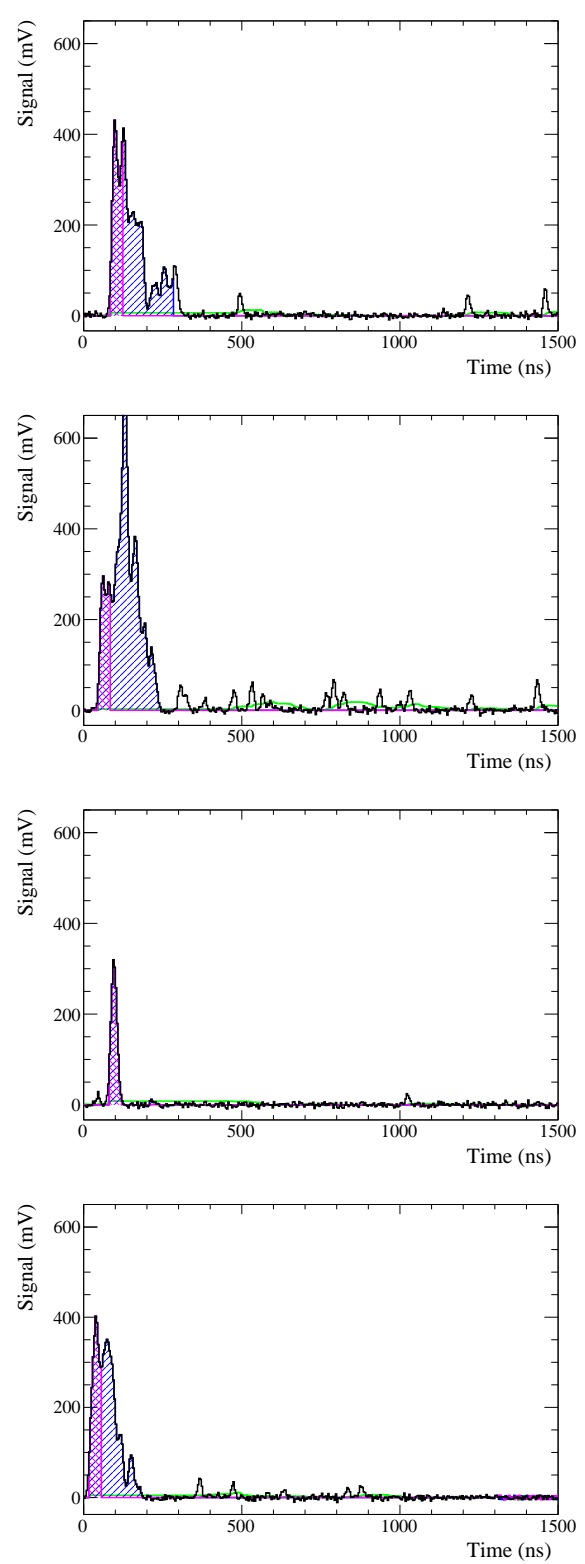
Figure 3 Simulated signals seen by the ^{6}Li detector in mV versus time for different combinations of signal and background events. The magenta left-diagonal-hatched region represents the Q_S portion of the signal, the blue right-diagonal-hatched region represents Q_L, and the green line (colour online) represents the average baseline. From top to bottom the plots show: a single signal event, a multiple signal event, a single background event, and a multiple background event.
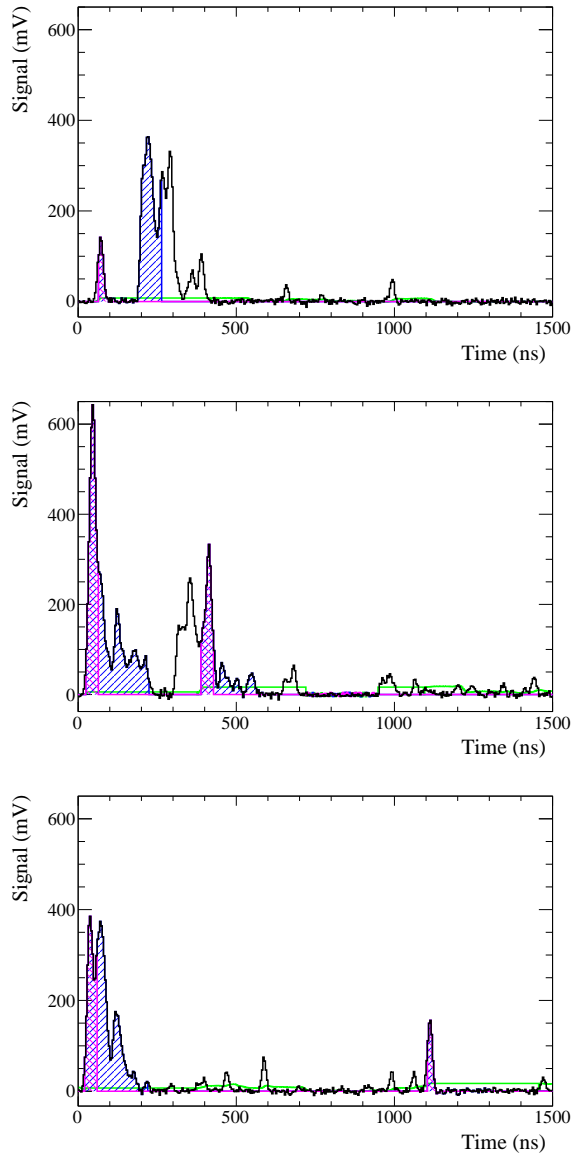
Figure 4 From top to bottom these plots show: a single signal plus single background event, a dead-time event, and a late-light re-trigger event.

gate is included in a single PDF. These multiple signal or multiple background PDFs could change shape if the rate of events is changed by over a few orders of magnitude, but is treated as fixed in estimating the detector performance.

Using a collection of randomly generated signal and background events, the PDFs for each of the signal types was generated. In the case of the single background event, it was possible to use the data from beam cycles with proton-beam off, when no UCN are produced. The rest of the PDFs were generated after tuning the simulation to match the data. In the simulation, the average number of photo-electrons per neutron capture, the fall time of the fast scintillation signal, the fall time of the long scintillation signal, and the average number of photo-electrons in the background were all tuned. In addition, the average charge in the signal measured by the detector, from each channel, was scaled to match the mean value in the simulation (as a gain matching).

The PDFs for the different combinations of signal and background are compared to data as shown in Fig. 5 and 6. A template fit of these PDFs to estimate amount of signal and background in the data is possible.

4 Estimate of the absolute detector efficiency and background contamination

In order to determine the UCN detection efficiency of the ^{6}Li active area of the detector, losses due to absorption in the front face, and neutrons lost due to the background rejection cuts need to be considered. In principle, one also has to take into account the spectrum of UCN that are being detected. Here we will assume that we want to know the efficiency for detecting UCN with kinetic energy above the effective Fermi potential of the GS20 lithium glass ($\sim$ 103.4 neV). Then if one has a known spectrum of UCN, the efficiency for detecting could be estimated as zero for the UCN below 103.4 neV, and the value we estimate here for those above 103.4 neV. Note that the Fermi potential of the GS30 (83 neV) is lower, and so should have negligible effect.

4.1 Detector effective area
The estimate of the detector's effective area comes from a photograph of the front face of the detector, where the side length of each of the tiles of ^{6}Li glass is 29.0 ± 0.1 mm. Using this known length the pixels in the photograph that make up the circular aperture of the detector are counted as the denominator, and the count of pixels containing lithium glass as the numerator. A photograph of the detector face is shown
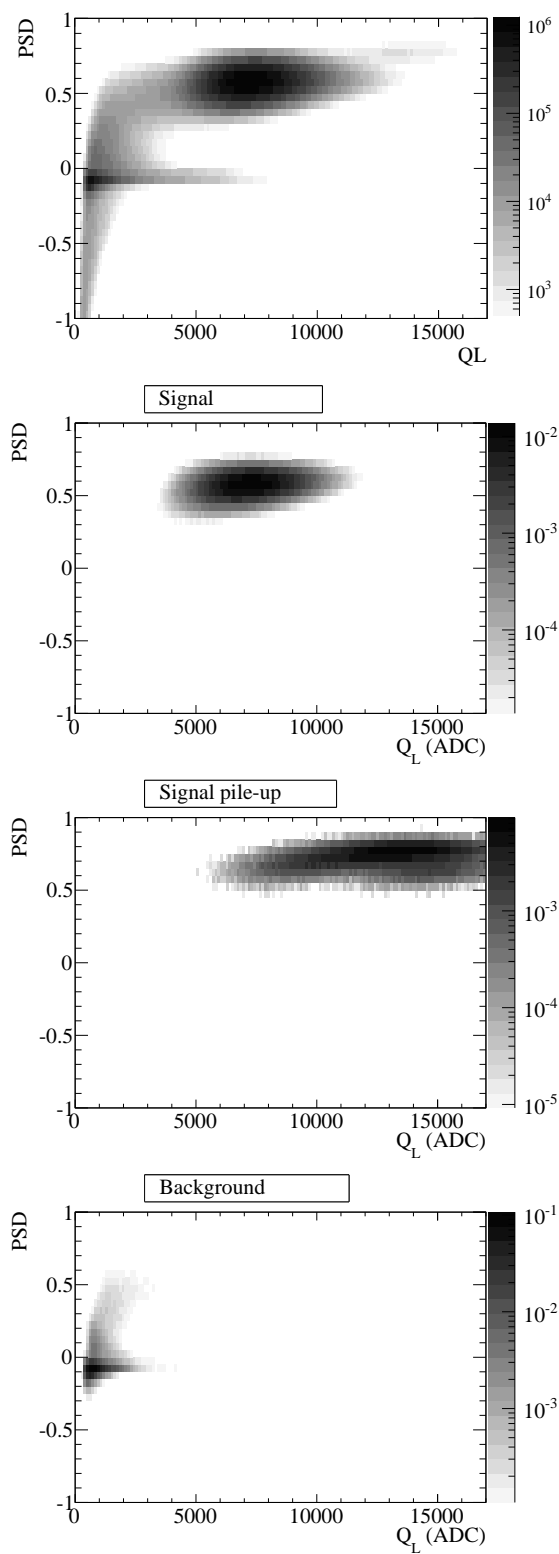
Figure 5 Event count (or relative event count) as a function of PSD and Q_L. From top to bottom: UCN data, single neutron simulation, multiple neutron simulation, and background (from data from cycles without proton beam).
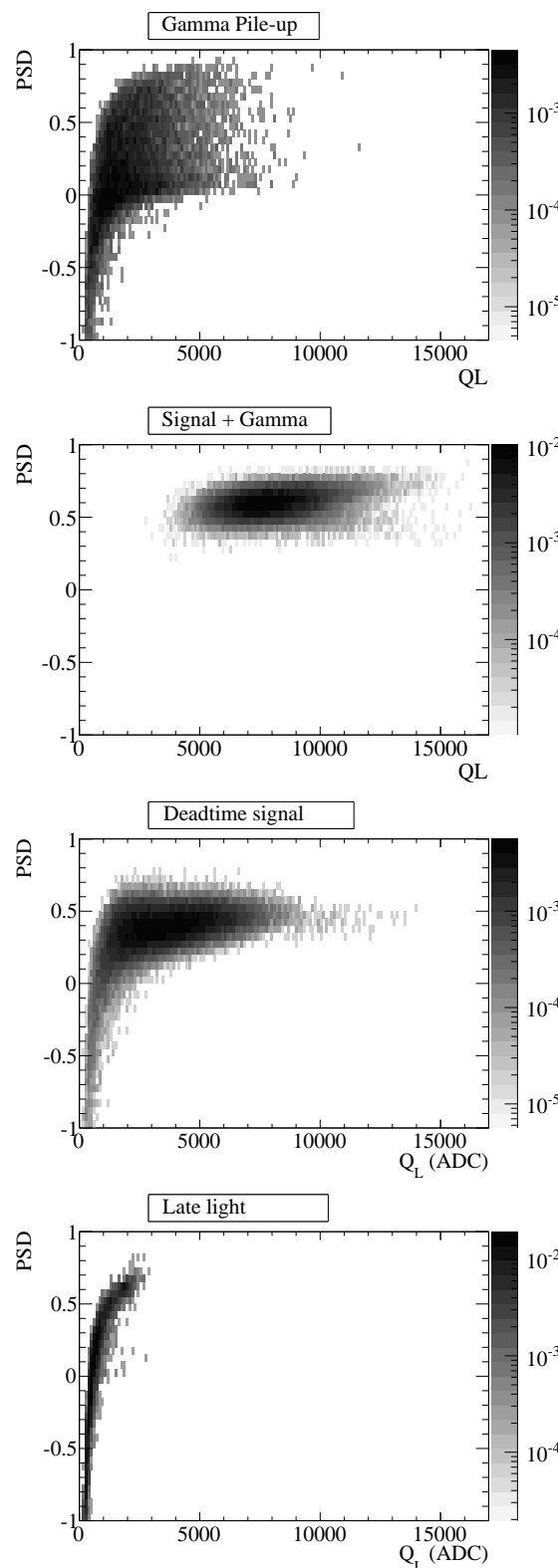
Figure 6 Event count (or relative event count) as a function of PSD and Q_L. From top to bottom: multiple background simulation, single neutron plus single background simulation, dead-time neutron simulation, and re-trigger on late light simulation.

in gray scale in Fig. 7. From this image the estimated active area of the detector is $97.4 \pm 0.1\%$ of the whole aperture.
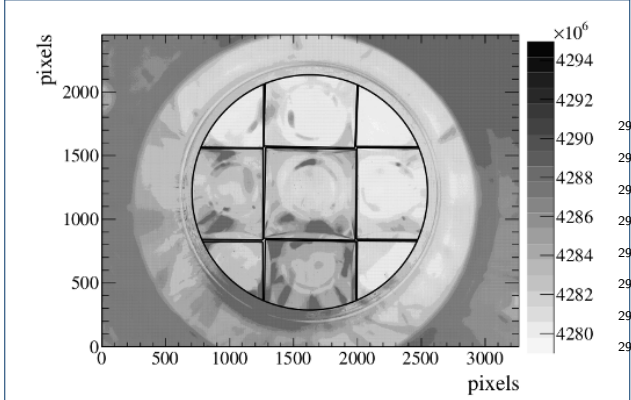
Figure 7 Image of the detector face used for estimating the areal efficiency of the detector. The detector aperture and edges of the lithium glass are identified by the black lines.

4.2 Estimation of UCN absorption in Li depleted layer

The cross section for absorption of UCN on ^{6}Li is $\sigma = (4.5 \pm 2.5) \times 10^5$ barns [17]. The company contracted to thin our samples of lithium glass has estimated our GS30 (lithium glass depleted in ^{6}Li) layer to be (55 ± 10) μm thick. Given that the lithium content in GS30 is $N = 2.4 \times 10^{-24}$ cm^{-3}, the absorption length, $\lambda = 1/(N\sigma)$, is $\lambda = 1.35 \pm 0.75$ cm. The fraction of UCN making it through our GS30 layer is calculated to be 99.34 ± 0.43 %.

Measurements of the transmission of UCN through different thicknesses of GS30 have been conducted by the LPC Caen group at the Institute Laue-Langevin in Grenoble [23]. Using their measurements for a 55 ± 10 μm GS30 layer the UCN transmission is $92.6^{+1.2}_{-1.8}\%$. The uncertainty is asymmetric due to the exponential nature of the attenuation through a layer with uncertain thickness. The measurements suggest that the UCN loss through a GS30 layer is not dominated by the ^{6}Li content, but by losses by up-scattering on other material of the glass such as Si and O.
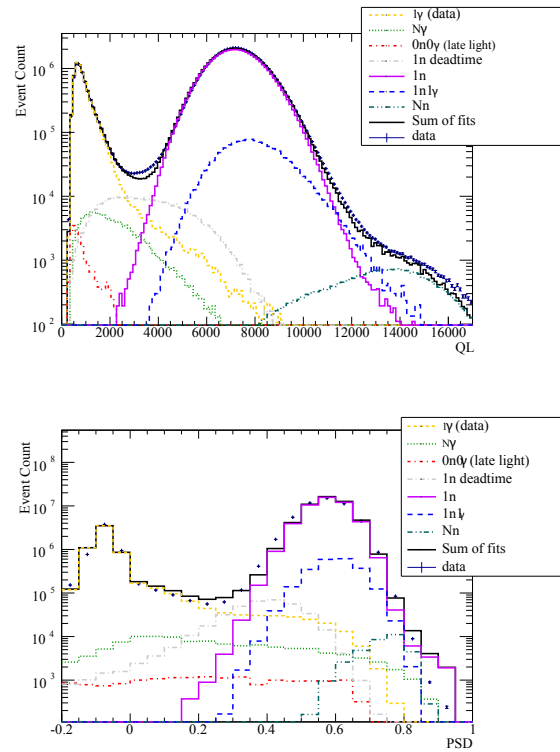
4.3 PSD cut efficiency and background rejection

The PSD and Q_L cut efficiency for keeping UCN, and background contamination remaining is estimated using an extended maximum likelihood fit of the PDF templates described in Section 3. The PDFs, binned in PSD and Q_L, are labelled as $P_i(PSD, Q_L)$, where $i = ($ 1n, Nn, 1γ, Nγ, 1n1γ, 1n deadtime, or 0n0$\gamma)$. The number of each type of event is estimated as N_i by minimizing a negative log likelihood that is calculated

as a sum over all M of the PSD^j and Q_L^j measurements in the data as:

$$-\ln(L) = \sum_i^7 N_i - \sum_j^M \ln \sum_i^7 P_i(PSD^j, Q_L^j). \quad (4)$$

A projection of the results onto the PSD and Q_L axes for one of these fits is shown in Fig. 8. All of the features seen in the data are reproduced in the fit, although the reduced chi-squared of the fit is rather poor. We attribute the differences to details that are not properly modelled, such as any contribution from light leaks, PMT after-pulsing, and differences in gain variation between the nine channels of the detector.

Figure 8 Template fit results in the one dimensional projections along the total event charge (top) and along the PSD (bottom).

Cut detection efficiency and background rejection estimates   Using the template fit, the neutron detection efficiency and background contamination are computed for different cut values in PSD and Q_L. The signal templates, in addition to single neutrons (1n), are taken to include multiple neutrons (Nn), deadtime neutrons (1n deadtime) and single neutron single

gamma ($1n1\gamma$) events. The background rates are extracted from the single gamma (1γ), late light ($0n0\gamma$), and multiple gamma ($N\gamma$) templates. If the total number of neutrons in the templates is N_n, and the number of neutrons above a given cut value is N_n^{cut}, then the neutron efficiency due to background rejection cuts is defined as:

$$\epsilon_n = \frac{N_n^{cut}}{N_n}. \tag{5}$$

If the number of events in the background templates above a given cut value is N_γ^{cut}, then the background contamination fraction is defined as:

$$\eta_\gamma = \frac{N_\gamma^{cut}}{N_n}, \tag{6}$$

and the background rejection as:

$$\epsilon_\gamma = 1 - \eta_\gamma. \tag{7}$$

Figure 9 shows the neutron efficiency and background contamination during the entire UCN cycle for two PSD cut values. For higher cut values, the efficiency is slightly reduced, but the background contamination is also reduced.

The rate of neutrons varies over the 300 second cycle of the UCN. To study the neutron detection efficiency and background contamination at different rates, the data was split into three time periods after the proton beam irradiation: high rate (0-10s), middle rate (10-40s), and low rate (40-270s). Each of these data sets was fit using the template fit and then the efficiency was calculated using the parameters from each fit. As shown in Fig. 10, the high rate data had more background contamination than the other rates, due to the larger fraction of events with pile-up effects. The lowest rate date data has a higher contamination than the mid-rate events, presumably due to the higher ratio of background to signal events. Using a cut on $Q_L > 3000$ ADC and $PSD > 0.3$, the neutron efficiency was $99.5 \pm 0.5\%$ and the background contamination was $0.3 \pm 0.1\%$.

The ^{6}Li detector therefore has a very good background rejection due to the signal shape variation between light-guide background and the scintillation events from the lithium glass.
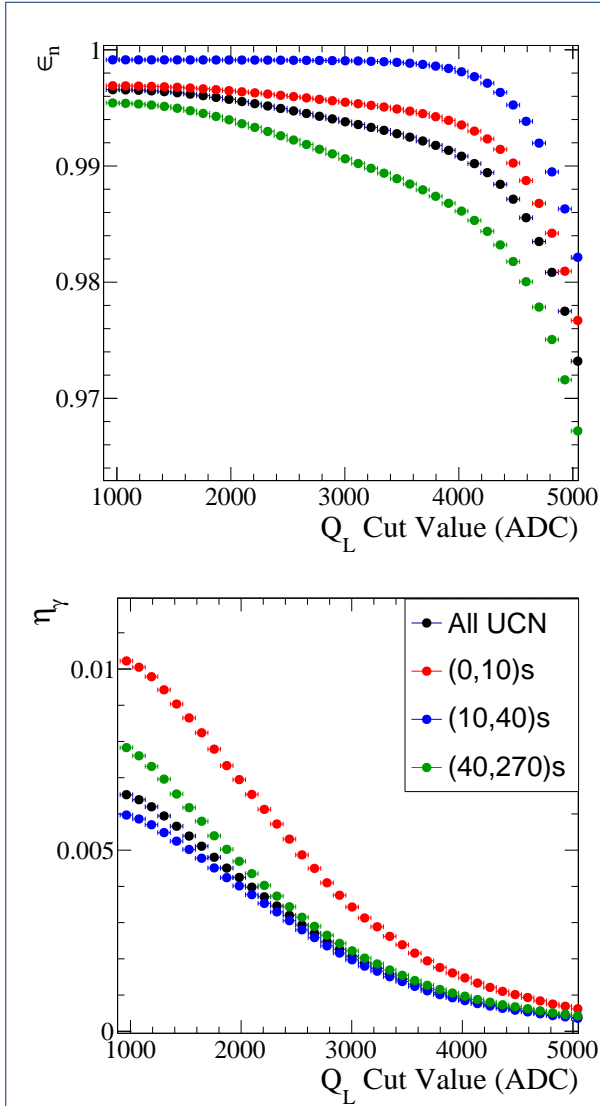
4.4 Overall Detector Efficiency Estimate

The overall detection efficiency, for the UCN rates and energies available at the West-2 beamport, including
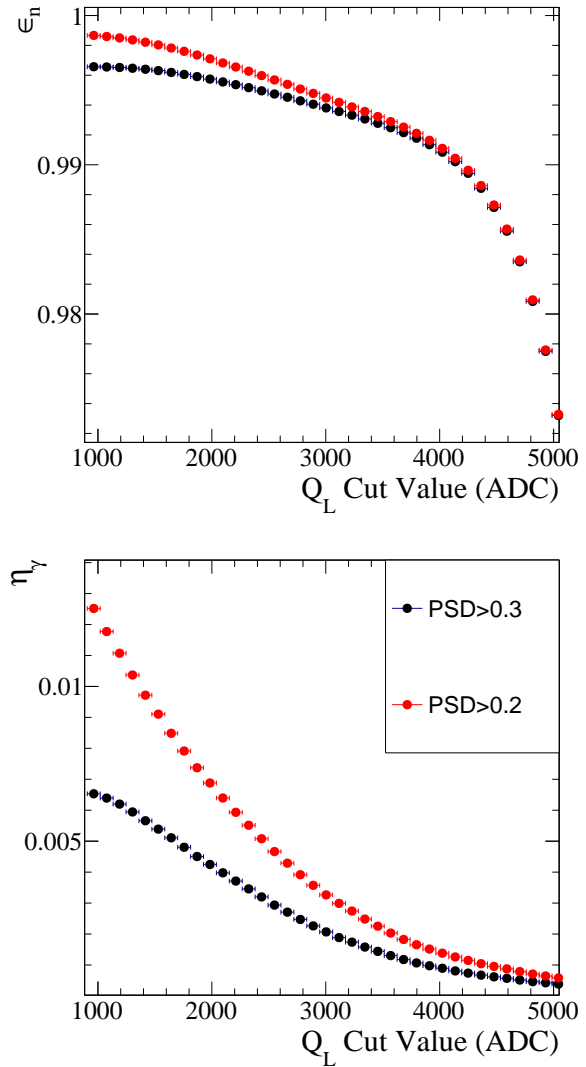
Figure 9 Neutron cut efficiency (top panel) and background contamination (bottom panel) for different cuts on Q_L. The red squares are with cut on PSD> 0.2, and the black circles are for a cut on PSD> 0.3

Figure 10 Neutron cut efficiency (top panel) and background contamination (bottom panel) for different times since the UCN production. The red boxes are for an average UCN rate of > 70 kHz over the first 10 s of UCN, the blue downward-triangles are for an average UCN rate of > 20 kHz over the next 30 s, and the green upward-triangles are for an average rate of < 10 kHz over the last 230 s.

all of the effects described in this section, is $89.7^{+1.3}_{-1.9}\%$, which is dominated by the uncertainty in the absorption in the GS30 layer. The rate dependence of the efficiency is below the 0.5% level. This uncertainty could be improved by applying what we know about the statistics of random signals and backgrounds to model the expected rates. This would represent an improvement to the simple fit with unconstrained fractions of different types of pile-up described in this paper. Some details of the statistics of random signal and background rates are provided in Appendix A.
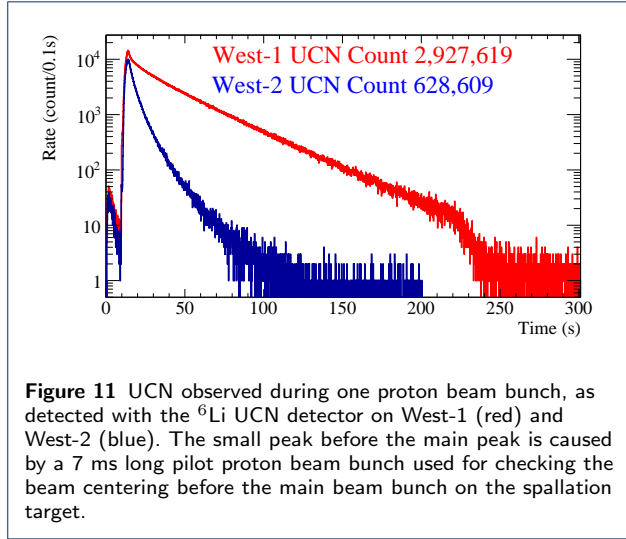
5 Relative rate comparison

We used the two beamlines called "West-1" and "West-2" at the PSI UCN source [24]. West-2, described in more detail in reference [24], offers the distinct feature that UCN have a dropping height of minimum 120 cm before reaching the detector. West-1 in a horizontal configuration provides UCN with energies starting above 54 neV given by the safety AlMg$_3$ foil in the beamline.

UCN rates on the West-1 beamline are typically a factor of 10 higher than on West-2. The operation mode during our measurements was given by the priority of the nEDM experiment measuring at the third beam-port. Typically, UCN were only delivered to the West-1 beamport after 30 seconds, when the nEDM experiment stopped its filling period. During the measurement period described here, the UCN source operation was using 3 second long proton beam bunches with a repeating period of 300 seconds . During and after the proton beam bunches the UCN can propagate down the beam line to the experiment area. Typical UCN detector rates during 300 second periods in West-1 and West-2 measured in Aug. 2015 with our scintillation detector are shown in Fig. 11.

Note that our detector's 75 mm diameter aperture does not match the 180 mm aperture of the West-1 beam-line, and that it can only see UCN above the Fermi potential of the scintillating glass (103.4 neV). This means that we see relatively more UCN from the vertical source, which has a spectrum starting at about 100 neV, matching our detector Fermi potential, than from the softer source of the horizontal West-1 beam. The PSI group has made measurements showing that on West-1, about 32% of the UCN are between 54 neV and 100 neV. Also, the two UCN cycles shown in the figure were taken on different days, and we know from measurements that during that time, the UCN source saw about a 15% decrease in the delivered UCN intensity [25]. Therefore, we expect to see less than the $10\times$ difference in UCN rate when comparing the distributions in Fig. 11.

The Q_L distribution from each of the nine channels of the detector, with a PSD cut at 0.3 to eliminate the

Figure 11 UCN observed during one proton beam bunch, as detected with the ^{6}Li UCN detector on West-1 (red) and West-2 (blue). The small peak before the main peak is caused by a 7 ms long pilot proton beam bunch used for checking the beam centering before the main beam bunch on the spallation target.

light-guide backgrounds, is shown in Fig. 12. These data are from twelve UCN cycles collected from the horizontal West-1 beamline. It is clear from these distributions that there is very little background remaining. The different numbers of counts seen make sense due to the geometry of the detector. The corner square tiles are shadowed the most by the round aperture of the detector opening, giving them the lowest count.

5.1 Channel to channel comparisons

In order to determine the rate stability of the detector, the first five channels' count (set A) per UCN cycle was compared to the last four channels (set B). During each UCN cycle on the West-1 beamline, the ^{6}Li detector counted about 3×10^6 neutrons, which has a statistical uncertainty of 0.06% (or 0.08% in each of two equal sized samples). A long overnight run containing 114 UCN cycles (9.5 hours) was taken to assess the rate stability. The count for each UCN cycle in each set of channels, and the ratio of counts per UCN cycle in set B over set A, is shown in Fig. 13. Note that there are four UCN cycles where the PSI nEDM experiment did not take the UCN, hence our detector did not have to wait after the proton beam bunch. Therfore, the number of UCN seen by our ^{6}Li detector during is higher than all of the rest of the cycles. Fitting the ratio of count rates to a constant yields an acceptable χ^2 per degree of freedom of 116.8 over 113, indicating that over the 9.5 hour data collection, the counts seen in these groups of the channels, relative to one another, is stable at the 0.08% level.

In order to compare the relative efficiency of each channel, the ratio of the count in each of the edge channels to the central channel was plotted. This was done for each of the UCN cycles, again showing that each channel had a count relative to the central channel
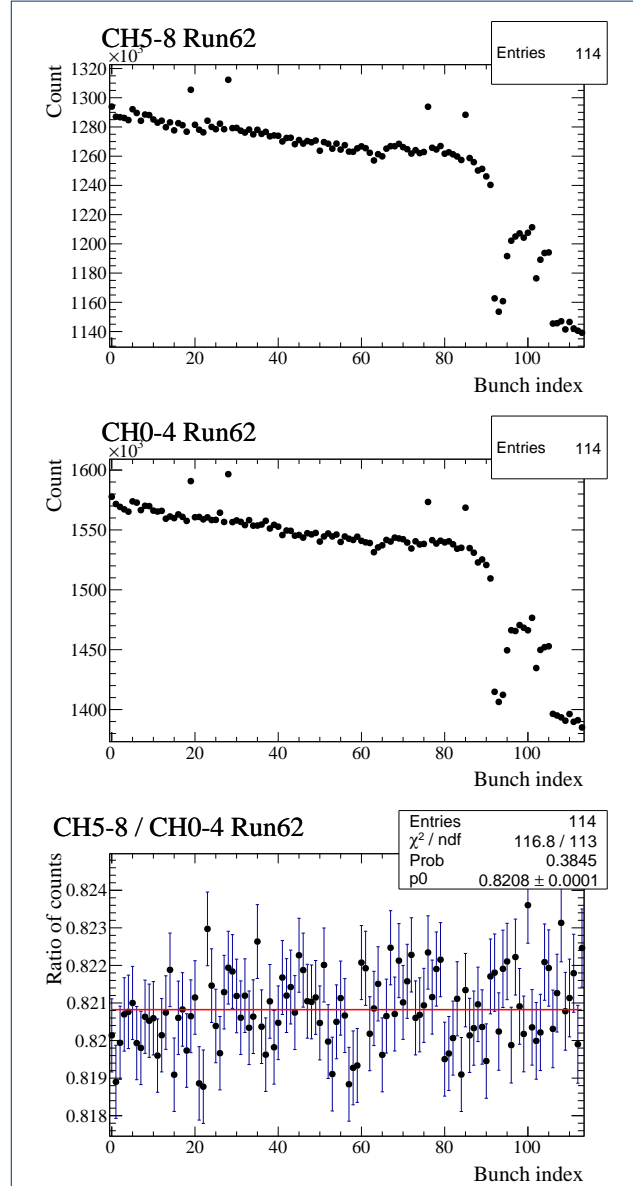
Figure 13 The top panel shows the Event count from set A (Channels 0-4) for each of the 300 s UCN cycles on West-2, the middle panel shows the event count from set B (Channels 5-8), and the bottom panel shows the ratio of counts from set B over set A.
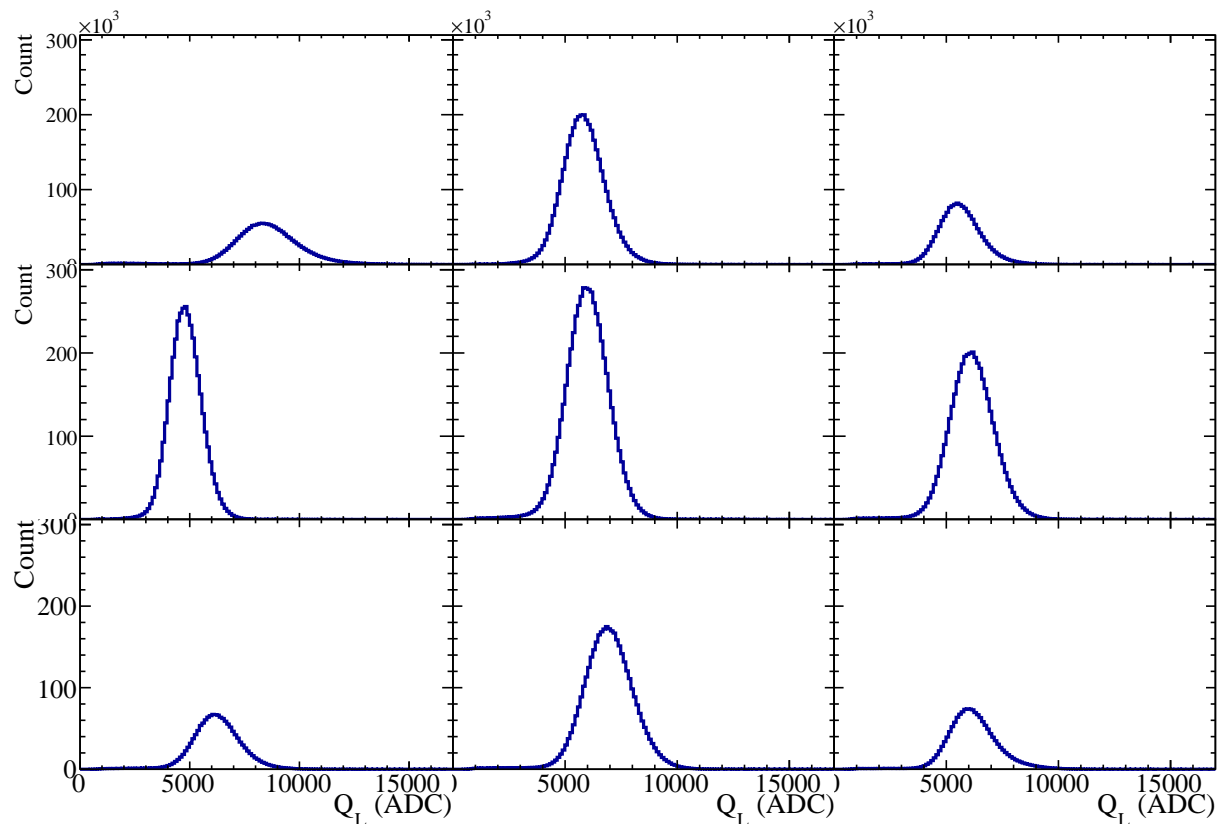
Figure 12 Event count per Q_L bin from each of the nine channels of the ^{6}Li scintillation detector from twelve cycles of UCN beam on the horizontal West-1 beamline. A cut on PSD> 0.3 has been applied to the events in this figure.

that is consistent with a constant efficiency. These relative rates were compared to the relative area exposed to UCN to get an estimate of the relative efficiency of the edge channels relative to the central channel. The relative count to the central channel, and relative area to the central channel are plotted in Fig. 14 for the same data shown in Fig. 13. These data are summarized in Table 1 and show there is a few percent, up to 5%, difference between the exposed area and the measured count rate. These differences could be due to a non-uniform UCN distribution reaching the detector, differences in the GS30 layer thicknesses, or the surface quality of each of the detector's tiles.

5.2 Comparison to Cascade detector

Both the Cascade and ^{6}Li detectors were connected individually to each of these ports and collected data. PSI also had a Y-configuration available which evenly split the beam between the detectors as shown in Figure 15. This allowed a more direct comparison of the UCN rates, and forms the basis of the comparison in this paper.

Figure 15 Configuration for splitting the UCN into two detectors. The Cascade detector is on the left and the ^{6}Li detector is on the right.

5.3 Cascade Detector

The Cascade UCN detector, typically used at PSI and other UCN facilities is a GEM-based neutron detector with a single 200 nm thick layer of ^{10}B deposited on a 100 μm thick aluminum entrance foil. The boron captures the neutron and releases an α and ^{7}Li particle,

$$^{10}B + n \rightarrow \alpha + {}^7Li. \tag{8}$$

An Ar/CO$_2$ mixture is used as a detection gas. Due to the low Z materials, this detector picks up negligible γ background. The employed detector has a 10×10 cm^2 square shaped sensitive area which is divided into 64 individually read out pixels. The detector comes with its own proprietary data acquisition system. The data acquisition is based on a complex pattern recognition algorithm which is performed online in the detector's FPGA electronics. This allows the software to define, within a given range, what patterns are accepted as a 'neutron' event. A stacked type of Cascade counter is more commonly used for cold and thermal neutron counting [26].

5.4 Overview of the Measurement Method

Both detectors were placed in the y-configuration at the West-2 port to allow for a comparison of the averaged UCN rate over the course of the beam cycle for both detectors for the same cycle. The timing calibration between the two detectors' Data AcQuisition (DAQ) was done at the few second level by comparing the time reported by the DAQ computers. A closer matching of the time in the analysis of the data was performed at about the 0.05 s level by aligning the times when the UCN rate was increasing after the main proton beam irradiation of the spallation target.

The gross timing is confirmed by looking at the total count of UCN seen in each detector per proton beam irradiation cycle. These counts are correlated as are the times when a proton beam irradiation is skipped and both detectors do not see UCN. Figure 16 shows the count of UCN detected in each 300 s cycle by each of the detectors.

Note that the ^{6}Li detector connects to the UCN source with a 75 mm aperture to the UCN guide, while the Cascade detector connects with a 70 mm aperture. To get a rough comparison of the two detectors, the count seen by the ^{6}Li detector is also shown scaled down by the ratio of areas (0.871). This comparison shows that the relative count of UCN from the PSI source was changing over the course of this data collection period, and that for the spectrum of UCN in this beamline for the 6Li detector is 10.279 ± 0.024(stat)%. The y-configuration is as direct a comparison as could be obtained, however simulations indicate there could be up to that large of a difference in expected UCN rate due to uncertainties in the initial UCN spectrum and the additional connectors required to reduce the 75 mm diameter guide to 70 mm diameter for the Cascade detector.

In addition to the comparison of the count for a whole 300 second cycle, the UCN detection rate in 0.1 second bins since the beginning of the beam cycle averaged over 132 beam cycles is compared, as shown in Fig. 17. This comparison includes the area normalization, and shows that the ^{6}Li detector appears to detect more UCN at higher rates at earlier times since
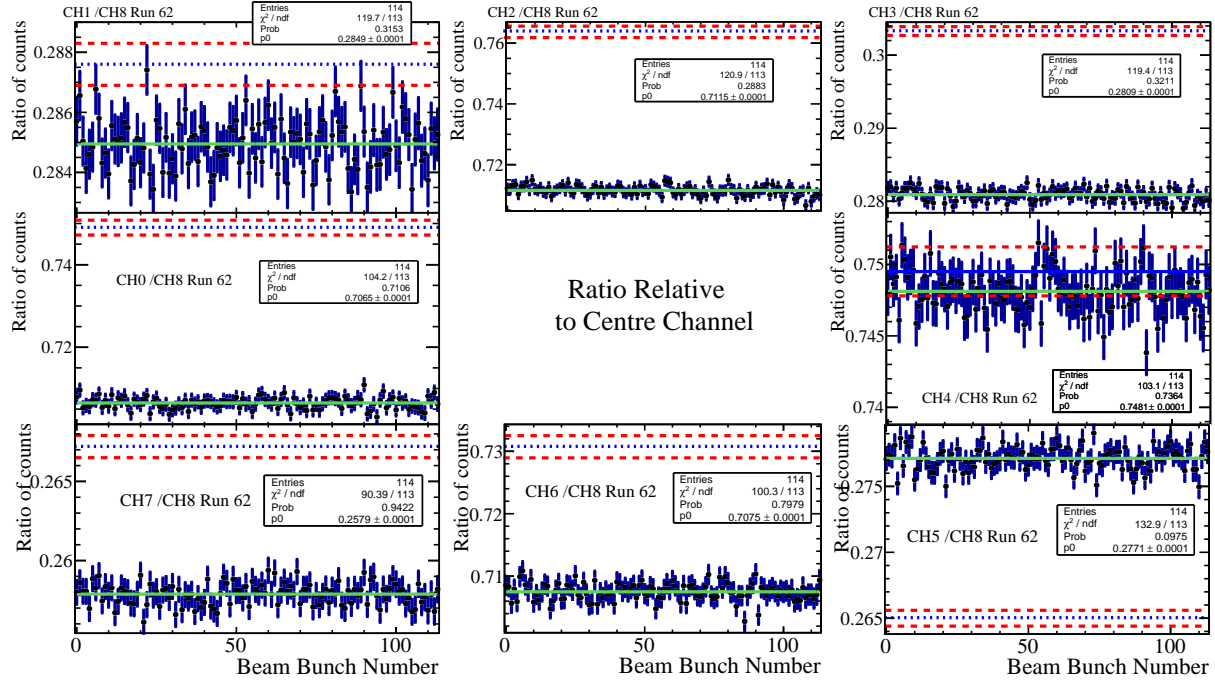
Figure 14 Count ratio of each channel relative to the central channel are shown (data points), and fit to a constant (green-solid lines). The relative area exposed to UCN is shown as a blue-dotted line with uncertainly given by the red-dashed lines.

Table 1 Relative to central channel (Ch.8) area compared to count of each of the detector channels

| Channel	Norm. area (A_N)	Norm. count (N_C)	($A_N - N_C$)
0	0.7490 ± 0.0018	0.7065 ± 0.0001	0.0425 ± 0.0018
1	0.2876 ± 0.0007	0.2849 ± 0.0001	0.0027 ± 0.0007
2	0.7634 ± 0.0018	0.7115 ± 0.0001	0.0519 ± 0.0018
3	0.3033 ± 0.0006	0.2809 ± 0.0001	0.0224 ± 0.0006
4	0.7495 ± 0.0017	0.7481 ± 0.0001	0.0014 ± 0.0017
5	0.2650 ± 0.0006	0.2771 ± 0.0001	-0.0121 ± 0.0006
6	0.7307 ± 0.0018	0.7075 ± 0.0001	0.0232 ± 0.0018
7	0.2672 ± 0.0007	0.2579 ± 0.0001	0.0093 ± 0.0007
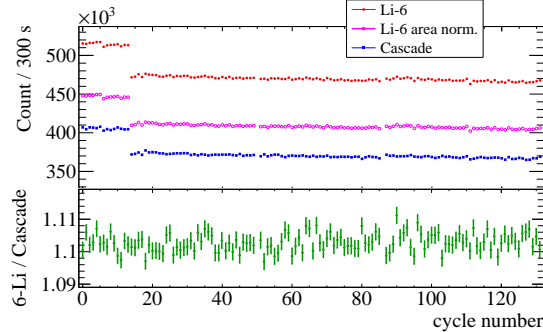
Figure 16 Detected UCN count per 300 second cycle is shown in the top panel for the ^{6}Li detector (red filled circles), Cascade detector (blue filled squares), and the area normalized ^{6}Li count (magenta open circles). The bottom panel shows the ratio of the area normalized count in the ^{6}Li detector to the Cascade detector (colour online).

the UCN production than the Cascade detector. We attribute the lower rate at later times to the difference in the Fermi potential of the two detectors. The ^{6}Li detector's lithium glass Fermi potential is 103.4 neV, while the Cascade detector has an Al window with an effective Fermi potential of 54 neV.

6 Conclusion

In this paper we have presented a newly developed ^{6}Li-based fast scintillation counter and a detailed electronics simulation which has been used to estimate the detector efficiency and background rejection for the data collected at the PSI UCN source. We estimate our detector efficiency is $89.7^{+1.3}_{-1.9}\%$, and background contamination to be $0.3 \pm 0.1\%$. Using comparisons of the rates of UCN from the different tiles of the ^{6}Li detector, and to the rate of UCN in a Cascade detector,
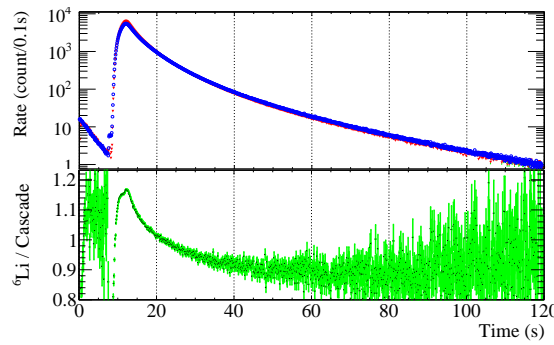
Figure 17 UCN Detection count per 0.1s averaged over 130 UCN cycles. The top panel shows an overlay of the area normalized ^{6}Li data in Red with the Cascade data in blue. The bottom plot shows a ratio of ^{6}Li count over Cascade count in each 0.1 s interval.

we have demonstrated that the detector is stable at the 0.08% level.

References

Author details
[1] Department of Physics, University of Winnipeg, 515 Portage Avenue, Winnipeg, Canada. [2] Laboratory for Particle Physics, Paul Scherrer Institute, CH5232, Villigen PSI, Switzerland. [3] TRIUMF, 4004 Wesbrook Mall, Vancouver, Canada. [4] Research Centre for Nuclear Physics, Osaka University, Osaka, Japan.

References
1. Pospelov, M., Ritz, A.: Electric dipole moments as probes of new physics. Annals of Physics **318** (2005)
2. Filippone, B.: New searches for the neutron electric dipole moment. Physics of fundamental Symmetris and Interactions at low energies **PSI2013** (2013)
3. Wohlmuther, M., et al.: The spallation target of the ultra-cold neutron source UCN at PSI. Nucl. Instr. and Meth. A **564** (2006)
4. A.P.Serebrov, et al.: New measurements of neutron electric dipole moment with double chamber EDM spectrometer. JETP Letters **99** (2014)
5. Serebrov, A.P., et al. Physics Procedia **17** (2011)
6. Kirch, K. AIP Conference Proceedings **1560** (2013)
7. Baker, C.A., et al. Physics Procedia **17** (2011)
8. Masuda, Y., et al. Physics Letters A **376** (2012)
9. Altarev, I., et al. Nuovo Cimento C **35** (2012)
10. Golub, R., Lamoreaux, S.K. Physics Reports **237** (1994)
11. Ito, T.M.: Plans for a neutron EDM experiment at SNS. J.Phys. Conf. Ser. **69** (2007)
12. Kawasaki, S.: 2nd generation He-II UCN source. Presented at CP violation in elementary particles and composite systems, RCNP, Osaka (2014)
13. Martin, J.W.: TRIUMF facility for a neutron electric dipole moment experiment. AIP Conference Proceedings **1560** (2013)
14. Lauss, B.: A new facility for fundamental particle physics: The high-intensity ultracold neutron source at the Paul Scherrer Institute. AIP Conference Proceedings **1441** (2012)
15. Lauss, B.: Commissioning of the new high-intensity ultracold neutron source at the paul scherrer institute. Hyperfine Interactions **211** (2012)
16. B.Lauss: Ultracold neutron production at the second spallation target of the Paul Scherrer Institute. Physics Procedia **51** (2014)
17. Ban, G., et al. Nucl. Instr. and Meth. A **611**(280) (2009)
18. Ban, G., et al. J. Res. Nat. Instr. Stand. Technol. **110** (2005)
19. Afach, S., et al.: A device for the simultaneous spin analysis of ultracold neutrons. European Physical Journal A **51** (2015)
20. Ban, G., et al.: Ultracold neutron detection with ^{6}Li-doped glass scintillators. arXiv:1606.07432 (2016)
21. Jamieson, B., Rebenitsch, L.A.: Determining the ^{6}Li doped side of a glass scintillator for ultra cold neutrons. Nucl. Instr. and Methods A **790** (2015)
22. Goeltl, L., et al. Eur. Phys. J. A **49** (2013)
23. Senoville, M.: Etude expérimentale d'un détecteur de neutrons capable de mésurer de fort taux de comptage. Rapport de stage de M1 Physique, Université de Caen Basse-Normande (2009)
24. Lauss, B.: UCN beamlines at PSI. PSI internal document, Paul Scherrer Institut (2014)
25. Ries, D.: Phd thesis no. 23671. PhD thesis, ETH Zuerich (2016)
26. Klein, M., Schmidt, C.J.: CASCADE, neutron detectors for highest count rates in combination with ASIC/FPGA based readout electronics. Nucl. Instr. and Methods in Particle Physics **628**(1) (2011)

Appendix A: Calculating the number of pile-up and dead-time events
Consider two independent rates of events, a rate of signal events and a rate of background events. Given a running time and detection window time, this section reviews the analytic calculation of the number of single signal, single background, the various combinations of multiple signal and background events, and the number of events during the dead-time.

A.1 Calculating the rates based on random Poisson processes
Consider a rate of signal events, R_{sig}. For a given running time, T, the number of expected signal events is $\nu_{\mathrm{sig}} = R_{\mathrm{sig}}T$. If a detector collects the signal over a gate with a width in time, t_{LG}, then in any of these gates the average number of events in that time interval is $n_{\mathrm{sig}} = R_{\mathrm{sig}}$. Each time the electronics triggers on a pulse from the detector it is dead for a time t_{dead} after the width of the collection gate.

As a final effect, for some fraction of the events detected, there is a second trigger (a re-trigger) on late light. The number of these events is some fixed fraction, f_{retrig}, of the single signal events. This fraction depends on the signal event threshold, but once determined for a given threshold, does not depend on the rate of events (only on the total number of events). The number of late light re-triggers is:

$$\nu_{\mathrm{retrig}} = f_{\mathrm{retrig}}\nu_{\mathrm{1sig}}. \tag{9}$$

The different combinations of events in a given running time, T, that are being considered are those that have:

1 a single signal event, ν_{1sig},
2 multiple signal events, $\nu_{N\mathrm{sig}}$,
3 a single background events, ν_{1bg},
4 multiple background events, $\nu_{N\mathrm{bg}}$,
5 a single signal plus a single background event, ν_{1sig1bg}, and
6 one or more signal events during the dead-time, ν_{dead}.

The rate of signal and background events each has an expected average number of events in any time interval that is a random process.

In any time interval, T, the number of single signal events measured, N_{1sig}, follows a Poisson distribution of the form:

$$P(N_{\mathrm{1sig}}, \nu_{\mathrm{1sig}}) = \exp\left(-\nu_{\mathrm{1sig}}\right)\frac{\nu_{\mathrm{1sig}}^{N_{\mathrm{1sig}}}}{N_{\mathrm{1sig}}!}.$$

The expected number of single signal events is defined to be:

$$\nu_{\mathrm{1sig}} = R_{\mathrm{sig}}T. \tag{10}$$

Similarly, the number of single background events, $N_{1\text{bg}}$, follows a Poisson distribution:

$$P(N_{1\text{bg}}, \nu_{1\text{bg}}) = \exp\left(-\nu_{1\text{bg}}\right) \frac{\nu_{1\text{bg}}^{N_{1\text{bg}}}}{N_{1\text{bg}}!}.$$

The expected number of single background events is defined to be:

$$\nu_{1\text{bg}} = R_{\text{bg}} T. \tag{11}$$

For the multiple signal events in a single gate, consider the probability of having more than one signal event in the time interval of the gate. In any randomly placed gate, the expected average number of signal events is $\bar{n}_{\text{sig}} = t_{\text{LG}} R_{\text{sig}}$. The gates are not randomly distributed, instead they occur if there already was a signal event that triggered the gate. Therefore for each of the $N_{1\text{sig}}$ signal events there is a probability of having more than one additional signal event of:

$$P(n_{\text{sig}} > 0, \bar{n}_{\text{sig}}) = 1 - P(0, \bar{n}_{\text{sig}}) = 1 - \exp\left(-\bar{n}_{\text{sig}}\right).$$

This is one minus the probability of having zero extra signal pulses in the gate. The probability above is multiplied by the average number of single signal events, giving the expected average number of multiple signal triggers:

$$\nu_{\text{Nsig}} = \nu_{1\text{sig}}(1 - \exp\left(-\bar{n}_{\text{sig}}\right)).$$

Plug in the number of expected events in a randomly placed gate to get the final result:

$$\nu_{\text{Nsig}} = \nu_{1\text{sig}}(1 - \exp\left(-t_{\text{LG}} \nu_{1\text{sig}}/T\right)). \tag{12}$$

Using a similar argument for multiple background events, on average, the result is:

$$\begin{aligned} \nu_{\text{Nbg}} &= \nu_{1\text{bg}}(1 - \exp\left(-\bar{n}_{\text{bg}}\right)) \\ &= \nu_{1\text{bg}}(1 - \exp\left(-t_{\text{LG}} \nu_{1\text{bg}}/T\right)). \end{aligned} \tag{13}$$

The number times we get a single neutron and a single gamma is calculated as a sum of two terms. The first term is the number of times we get a single signal event times the probability of getting a single background event in a randomly placed gate. The second term is the number of times we get a single background event times the probability of getting a single signal event in a randomly placed gate. On average the number of these events is:

$$\begin{aligned} \nu_{1\text{sig}1\text{bg}} = {} &\nu_{1\text{sig}} \exp\left(-t_{\text{LG}} \nu_{1\text{bg}}/T\right) t_{\text{LG}} \nu_{1\text{bg}}/T + \\ &\nu_{1\text{bg}} \exp\left(-t_{\text{LG}} \nu_{1\text{sig}}/T\right) t_{\text{LG}} \nu_{1\text{sig}}/T. \end{aligned} \tag{14}$$

Finally, the number of dead-time signal events, ν_{dead}, can be calculated in a similar manner to the pile-up, ν_{Nsig}. Assume the total number of triggers is dominated by the single signal or single background events: $\nu_{1\text{sig}} + \nu_{1\text{bg}}$. For each of these triggers, the average number of signal events during a dead time is $\bar{n}_{\text{dead}} = t_{\text{dead}} R_{\text{sig}}$. Each of the triggers has a Poisson probability of having one or more signal events during the dead time:

$$\begin{aligned} P(n_{\text{dead}} > 0, \bar{n}_{\text{dead}}) =& 1 - P(0, \bar{n}_{\text{dead}}) \\ =& 1 - \exp\left(-\bar{n}_{\text{dead}}\right). \end{aligned}$$

Again, this is just one minus the probability of having zero extra signal pulses in the time period after any gate. Multiply the above probability

times the number of triggers, and we expect, on average, to have the number of dead-time neutrons:

$$\nu_{\text{dead}} = (\nu_{1\text{sig}} + \nu_{1\text{bg}}) \cdot (1 - \exp\left(-t_{\text{dead}} \nu_{1\text{sig}}/T\right)). \tag{15}$$

A.2 Calculations to test the rate equations

In this section plots of the ratio of the number of events to the total number of events as a function of signal rate and background rate are plotted. These plots are made as a contour map, with y-axis being the signal rate, R_{sig}, the x-axis being the background rate, and the z-axis being the fraction of the triggers of the given type. These plots are made for each of the seven categories of events.

For these plots we will use the settings that were used for the digitizer in the measurements at PSI. The relevant settings are, $t_{\text{LG}} = 200$ ns, $t_{\text{dead}} = 150$ ns, and $f_{\text{retrig}} = 0.1$. For these gate times, consider what happens when there is a high signal rate of $R_{\text{sig}} = 1/t_{\text{LG}} = 5$ MHz with no background. After an arbitrary $T = 10$ s of running at this rate the number of single signal events is $\nu_{1\text{sig}} = R_{\text{sig}} T = 10^7$ events. On average the number of times there is a multiple signal events is given by Eq. 12:

$$\nu_{\text{Nsig}} = 10^7 (1 - \exp\left(-2^{-7} \text{ s } \cdot 10^7/10 \text{ s}\right)) = 1.8 \times 10^6. \tag{16}$$

This seems reasonable that there would be a large fraction of the events ($\sim 18\%$) that would have more than one neutron.

In calculating the fractions of events we use for the denominator, the total average (expected) number of triggers as a function of rate:

$$\nu = \nu_{1\text{sig}} + \nu_{N\text{sig}} + \nu_{1\text{bg}} + \nu_{N\text{bg}} + \nu_{1\text{sig}1\text{bg}} + \nu_{\text{dead}} + \nu_{\text{retrig}}. \tag{17}$$

In equation 17 each term can be calculated using Eqs. 9 to 15, which may depend on the signal and background rates. For example the fraction of single signal events is then given by:

$$f_{1\text{sig}} = \frac{\nu_{1\text{sig}}}{\nu}. \tag{18}$$

Similar expressions can be written for the fractions of each of the event types. Fig. 18 and Fig. 19 show the fraction of each type of event as a function of signal and background rate.
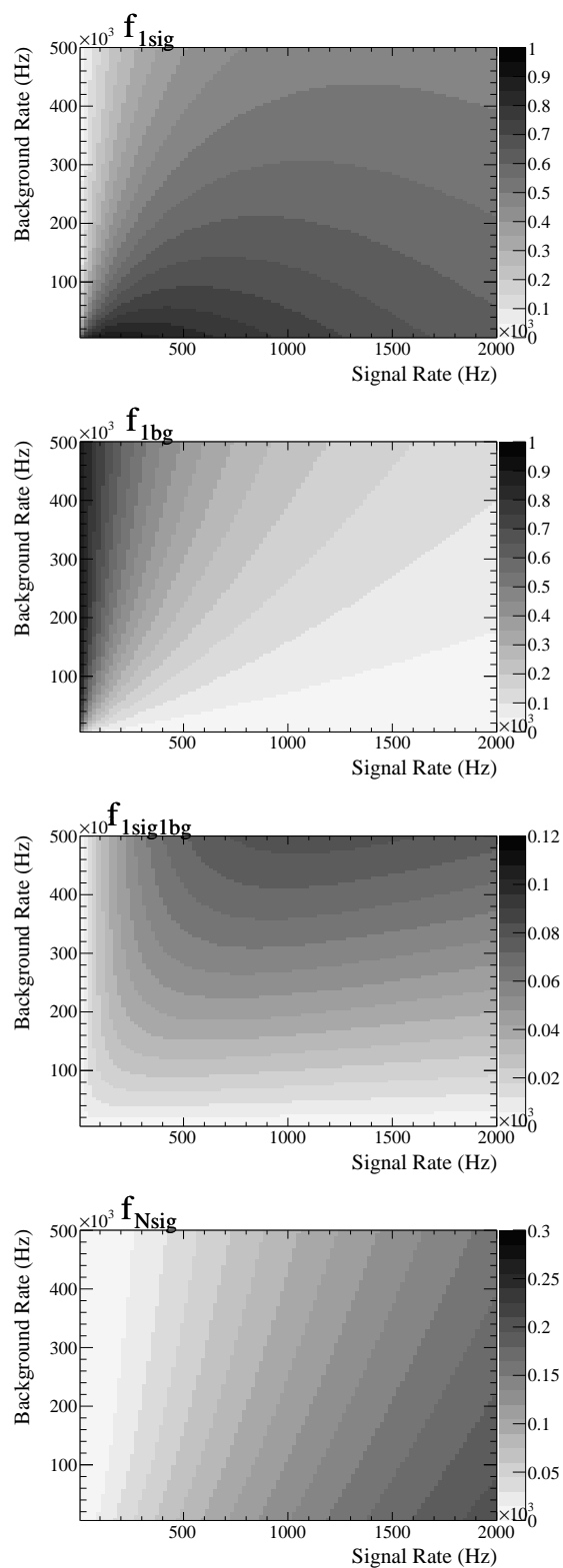
Figure 18 Fraction of events as a function of rate, going from top to bottom are for: single signal events, single background events, 1 signal and 1 background events, and multiple signal events.
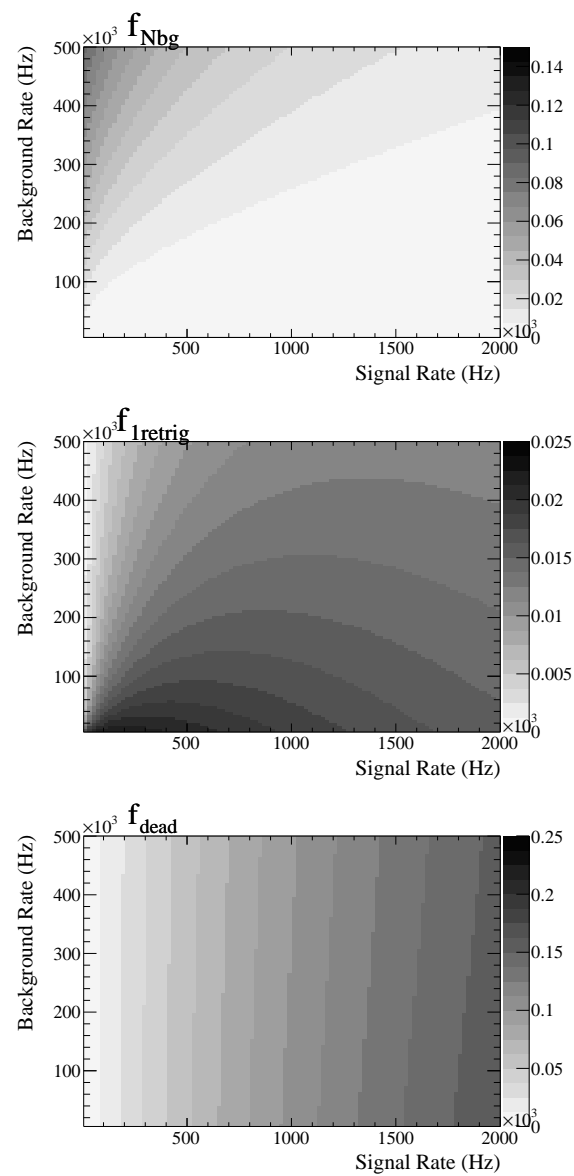
Figure 19 Fraction of events as a function of rate, going from top to bottom are for: N background events, re-trigger on late light (set at 2.5%), and dead time signal events.